Hybrid Catalyst Coupling Single-Atom Ni and Nanoscale Cu for Efficient CO_2 Electroreduction to Ethylene

Zhouyang Yin,[†] Jiaqi Yu,[‡] Zhenhua Xie,[§] Shen-Wei Yu,[†] Liyue Zhang,[†] Tangi Akauola,[†] Jingguang G. Chen,*[,§] Wenyu Huang,*[,‡] Long Qi,*[,∥] and Sen Zhang*[,†]

[†]Department of Chemistry, University of Virginia, Charlottesville, Virginia 22904, United States

[‡]Department of Chemistry, Iowa State University, Ames, Iowa 50011, United States

[§]Department of Chemical Engineering, Columbia University, New York, New York 10027, United States

[∥]U.S. DOE Ames Laboratory, Iowa State University, Ames, Iowa 50011, United States

KEYWORDS: hybrid catalyst, CO_2 reduction, electrocatalysis, ethylene, in-situ

ABSTRACT: A hybrid catalyst with integrated single-atom Ni and nanoscale Cu catalytic components is reported to enhance the C-C coupling and ethylene (C_2H_4) production efficiency in the electrocatalytic CO_2 reduction reaction (eCO_2RR). The single-atom Ni anchored on high-surface-area ordered mesoporous carbon enables high-rate and selective conversion of CO_2 to CO in a wide potential range, which complements the subsequent CO enrichment on Cu nanowires (NWs) for the C-C coupling to C_2H_4. *In situ* surface-enhanced infrared absorption spectroscopy (SEIRAS) confirms the substantially improved CO enrichment on Cu once its integration with single-atom Ni. Also, *in situ* X-ray absorption near edge structure (XANES) demonstrates the structural stability of the hybrid catalyst during eCO_2RR. By modulating hybrid compositions, the optimized catalyst shows 66% Faradaic efficiency (FE) in an alkaline flow cell with over 100 $mA{\cdot}cm^{-2}$ at -0.5 V vs. reversible hydrogen electrode, leading to a five-order enhancement in C_2H_4 selectivity compared with single-component Cu NWs.

INTRODUCTION

Reaching net-zero CO_2 emission by 2055 is critical to limiting global warming to 1.5 ℃ above the pre-industrial periods, as emphasized by the Intergovernmental Panel on Climate Change (IPCC).[1] The utilization of CO_2 as an alternative C_1 feedstock for commodity chemical production is a promising strategy to reduce and even eliminate the dependence on fossil fuel resources for a rapid decarbonization.[2,3] Compared with conventional thermal conversion of CO_2, eCO_2RR is advantageous in terms of prospects for distributed chemical manufacturing under ambient conditions, and the direct use of clean electrical energy and the proton source in water.[4–7] In the past few decades, eCO_2RR has been extensively investigated, and among various catalytic materials studied, Cu is the most appealing one due to its ability to enable C-C coupling to produce C_2+ hydrocarbons and oxygenates that are more valuable than C_1 products (CO, CH_4, formate).[8–10] Substantial efforts have been devoted to tailoring Cu catalysts to enhance the C_2+ production, including tuning crystalline plane of Cu (e.g., (100))[11,12] or boundary/stepped Cu surface,[13-15] alloying with other elements,[16,17] adjusting Cu oxidation state,[18-20] surface ligand modification,[21] synthesizing Cu-based metal-organic frameworks,[22-25] and modulating catalyst-electrode integration.[20,26,27] To get more insights of the C-C bonding, a variety of in-situ characterization methods have also been developed.[28-33] Despite some progress, Cu-based catalysts still remain low in energy efficiency and product selectivity, especially when targeting one specific C_2+ product rather than a mixture.[6,34,35]

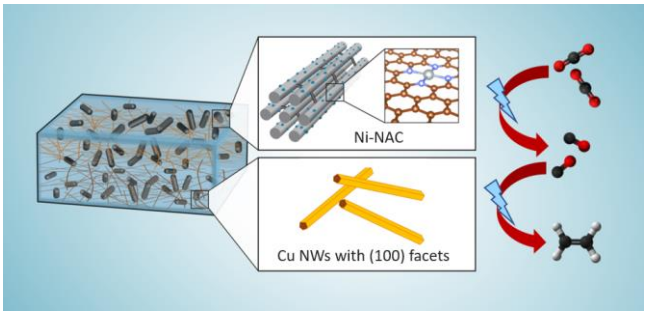

Figure 1. Schematic illustration of modular design of Cu/Ni-NAC hybrid catalyst for tandem catalysis.

Here we report a hybrid catalyst with two functional modules, single-atom Ni and nanoscale Cu being properly coupled to facilitate selective production of C_2H_4 in eCO_2RR (Figure 1). C_2H_4 is one of the largest volume organic chemicals produced in petrochemical industry, and is broadly used to synthesize plastics and other chemicals.[36] Previous theoretical work suggested that the adsorbed *CO is an

important intermediate for the subsequent C-C coupling, and experimentally, Cu with the (100) catalytic surface is among such catalysts.[37–40] However, Cu is kinetically sluggish in the CO_2-to-CO step, which limits the surface coverage of *CO and results in high overpotential and low selectivity for C_2H_4 production.[41] In principle, a hybrid catalyst that cascades CO_2-to-CO and CO-to-C_2H_4 conversions should greatly favor the C_2H_4 production, but this requires these two complementary conversion steps to have matching overpotentials for the maximized synergy. Very recently, we have developed a single-atom Ni catalyst anchored on nitrogen assembly carbon (Ni-NAC) that can catalyze CO_2-to-CO with more than 90% Faradaic efficiency (FE) at a wide potential range, due to the enhanced mass transfer from high-surface area ordered porous architecture and the abundant single-atom Ni catalytic centers.[42,43] We envision that such a single-atom Ni-NAC material is an ideal candidate to complement Cu for the tandem conversion. Our results show that, by properly assembling single-atom Ni-NAC and Cu NWs with dominant {100} surface facets, a high-rate eCO_2RR with a 66% FE to C_2H_4 at moderate potential {-0.5 V vs. reversible hydrogen electrode (RHE)} is obtained. *In situ* SEIRAS provides direct evidence of substantially enhanced CO enrichment on Cu in the hybrid catalyst. Our work highlights the modular design of hybrid catalysts to optimize reaction kinetics for eCO_2RR and potentially for other complex reactions.

RESULTS AND DISCUSSION

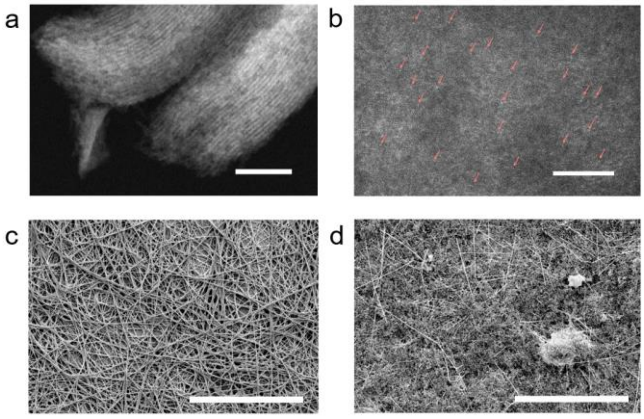

Figure 2. (a) STEM HAADF image of Ni-NAC materials showing ordered porous structure (scale bar = 100 nm). (b) The atomic resolution STEM image of Ni-NAC. Red arrows illustrate single-atom Ni sites (scale bar = 5 nm). (c, d) SEM images of Cu NWs (c) and Cu/Ni-NAC hybrid catalyst (d) (scale bar = 50 μm).

Catalyst Preparation and Characterization. The single-atom Ni-NAC and Cu NWs were synthesized separately, according to the reported methods (Supporting information, SI).[37,42] As shown in Figure S1, the as-synthesized Cu NWs have a diameter of ~50 nm and a length of several to tens of μm. The face-centered cubic (fcc) metallic Cu structure is confirmed using X-ray diffraction (XRD) (Figure S2). The surface of Cu NWs is mainly composed of {100} facets (Figure S3), which have been proven to be active for the CO reduction to C_2H_4.[11,44] The single-atom Ni-NAC possesses an ordered mesoporous architecture, as indicated by the aberration-corrected scanning transmission electron microscopy (STEM) high-angle annular dark field (HAADF) image (Figure 2a). The formation of single-atom Ni is also visualized in HAADF-STEM image (Figure 2b). After Cu NWs and Ni-NAC were successfully synthesized, they were mixed in hexanes under sonication to generate the hybrid catalysts (Figure 1). As shown in the scanning electron microscopy (SEM) image in Figure 2c, before assembly, high-purity Cu NWs intersect with each other. After assembly (Figure 2d), the Cu NWs are uniformly embedded in the matrix of Ni-NAC and Vulcan carbon, suggesting that Cu NWs and Ni-NAC are in close contact. In addition, the morphology of Cu NWs is not changed after the formation of the hybrid catalysts.

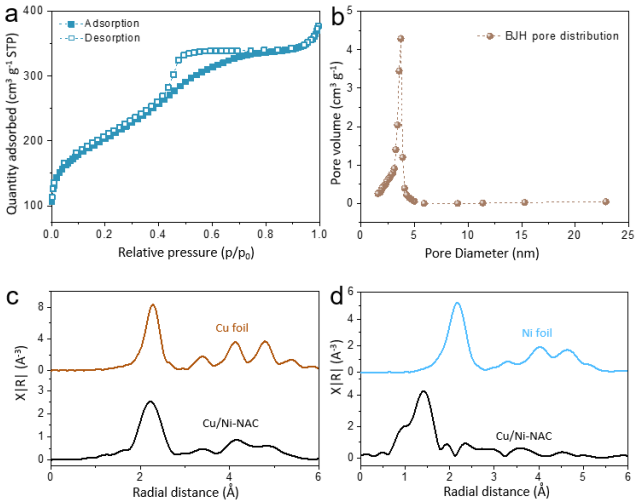

Figure 3. (a) Nitrogen sorption isotherm analysis of Ni-NAC. (b) Pore distribution of Ni-NAC. (c, d) R-space plots of Cu (c) and Ni (d) K-edge EXFAS of metal foil standard and hybrid catalyst.

Besides electron microscopy for morphology characterization, N_2 physisorption measurement shows that the surface area of single-atom Ni-NAC sample reaches 718 $m^2 g^{-1}$ due to the uniform (Figure 3a) and interconnected 3.0 nm pores (Figure 3b). Consistent with our previous report, the Ni-NAC sample presents single-atom Ni on the graphitic N-doped carbon with a Ni loading of 1.7 wt.% while no Ni nanoparticles are formed, as interpreted from the ICP results, the XRD pattern (Figure S4), and extended X-ray absorption fine structure (EXAFS) measurement (discussed below). To understand the atomical coordination structure of the hybrid material, we performed *ex situ* EXAFS measurements of Cu/Ni-NAC, as summarized in Figure 3c and d. The R-space plot of the hybrid catalyst is consistent with the Cu foil standard, in which a Cu-Cu scattering pathway is observed at 2.2 Å, a typical feature for *fcc* Cu structure (Figure 3c). Unlike the EXAFS of Cu, the main peak in the R-space plot of Ni locates at 1.45 Å, which is identical to the Ni-N peak in reported Ni-phthalocyanine (Pc) standard (Figure 3d).[45] Compared with the Ni foil reference, there is no detectable Ni-Ni peak in the hybrid

catalyst. Therefore, the hybrid catalyst contains both single-atom Ni and continuous Cu metallic structures.

In order to investigate the bi-component effect and avoid CO deficiency or overproduction, Cu NWs and Ni-NAC with different ratios are assembled and evaluated. Cu NWs: Ni-NAC: Vulcan carbon weight ratio are controlled to be 2:1:1 (Cu/Ni-NAC 2:1), 5:1:4 (Cu/Ni-NAC 5:1), and 10:1:9 (Cu/Ni-NAC 10:1), where the eCO_2RR-inert carbon support (Vulcan carbon) is added to maintain the conductivity of the catalysts and the carbon (Vulcan carbon + Ni-NAC)/Cu ratio is unchanged (1:1).

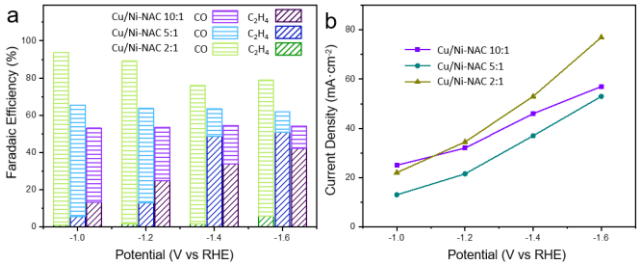

Figure 4. eCO_2RR (a) products distribution and (b) current density of Cu/Ni-NAC hybrid catalysts in different potentials.

Electrochemical Performance. We first used a H-cell in a neutral electrolyte (0.5 M $KHCO_3$) to evaluate the impact of different compositions of Cu/Ni-NAC for the eCO_2RR, where online gas chromatograph (GC) and nuclear magnetic resonance (NMR) were employed to analyze gas and liquid products, respectively. The typical GC and NMR spectra are displayed in Figure S5 and S6. As summarized in Figure 4a, the Cu/Ni-NAC 2:1 sample shows the highest FE toward CO among the three hybrid catalysts, indicating that a high ratio of single-atom Ni module leads to CO overproduction. As a result, although the C_2H_4 yield becomes higher as the overpotential increase, the highest C_2H_4 FE for the same catalyst is still less than 10%. We found that increasing the relative content of Cu NWs in the hybrid catalyst significantly enhances C_2H_4 FE. Using the Cu/Ni-NAC 5:1 catalyst, the highest C_2H_4 FE could reach 50% at -1.4 V vs RHE, but only 14% of C_2H_4 is obtained at -1.2 V. With more Cu NWs incorporated, Cu/Ni-NAC 10:1 produces 23% of C_2H_4 at -1.2 V, but has slightly lower FE at higher overpotentials. The current densities of these hybrid catalysts are displayed in Figure 4b. From -1.2 to -1.6 V, Cu/Ni-NAC 2:1 has the highest current density (up to 80 mA·cm^{-2}) due to the highest catalyst loading amount. Although the Cu NWs and Ni-NAC loading are lowered in Cu/Ni-NAC 5:1 and Cu/Ni-NAC 10:1 due to increased use of Vulcan carbon, their current densities are just slightly lower with greatly enhanced C_2H_4 FE. Taking both C_2H_4 FE and current density into consideration, Cu/Ni-NAC 10:1 stands out with the optimized performance and is specifically discussed below for *in situ* spectroscopy studies and flow-cell testing.

***In situ* Spectroscopy.** To confirm our hypothesized coupling mechanism in hybrid catalysts, we used *in situ* SEIRAS to elucidate the reaction intermediates and pathways during the eCO_2RR. We deposited a thin film of Au nanoparticles on the silicon attenuated total reflection crystal that serves as both a working electrode and a surface enhancement layer to improve intermediate signals.[46] Then, our catalysts were uniformly spin-coated on the Au-modified silicon crystal, and we ensured that Au film was fully covered to avoid Au interference in eCO_2RR. As shown in Figure 5a, the hybrid Cu/Ni-NAC catalyst exhibits two strong CO adsorption peaks at 2050 and 1950 cm^{-1} during the negative scan, representing clear evidence that *CO generated from Ni-NAC module is transferred and enriched on the surface of Cu NWs for the subsequent C-C coupling. As the potential becomes more negative, the atop-bound *CO band intensity (2050 cm^{-1}) decreases, and the bridge-bound CO peak (1950 cm^{-1}) increases, which is in accordance with previous report.[47] In contrast, with Cu NWs as the catalyst, there are no peaks associated with bridge-bound CO were observed, and a small atop-bound CO peak only appeared after -0.8 V (Figure 5b), indicating a low coverage of *CO on Cu NWs during the eCO_2RR. In addition, control experiments with only Ni-NAC catalyst were also tested using *in situ* SEIRAS under the same condition (Figure S7), and there is no detectable *CO peak, suggesting that the effective integration of Ni-NAC and Cu NWs are essential for such a strong *CO enrichment phenomenon.

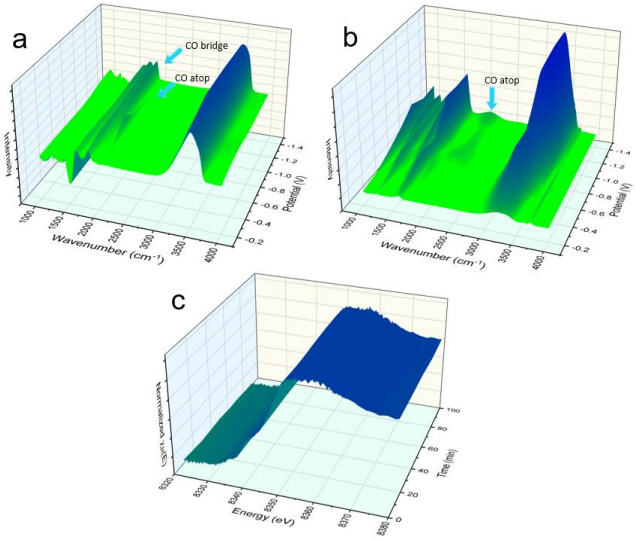

Figure 5. (a, b) *In situ* SEIRAS spectra of Cu/Ni-NAC (a) and Cu NWs (b) catalysts under eCO_2RR conditions. (c) *In situ* XANES of Ni K edge of Cu/Ni-NAC eCO_2RR conditions.

Furthermore, Ni K-edge XANES spectra were also analyzed and summarized in Figure 6. It is clearly seen that, for both as-prepared and post-electrolysis, *ex situ* Ni K-edge XANES spectra of the hybrid catalyst are distinctive from Ni foil but identical to Ni-NAC. In addition, under *in situ* conditions for eCO_2RR, *in situ* Ni K-edge spectra remain unchanged (Figure 5c), confirming the high stability of single-atom Ni structures in the hybrid catalyst.

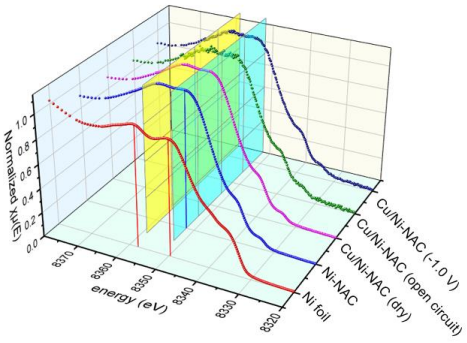

Figure 6. XANES results of Cu/Ni-NAC under different conditions.

Performance Optimization with Flow Cell. Changing the neutral-pH electrolyte to alkaline solutions should suppress the competing hydrogen evolution reaction (HER) and boost the C-C coupling reaction in eCO_2RR; however, it is likely to cause bicarbonate/carbonate formation and crossover issue in the full electrolyzer. To minimize CO_2 and alkaline solution reaction and to optimize electrolyzer performance, we assembled a flow cell with Cu/Ni-NAC 10:1 catalyst-modified gas diffusion electrode and 1 M or 10 M KOH electrolyte (Figure S8). As shown in Figure 7a, in 1 M KOH Cu/Ni-NAC 10:1 starts to produce more than 15% of C_2H_4, and the C_2H_4 FE keeps increasing with the overpotential. At -0.9 V, the C_2H_4 FE reaches a plateau of 53%. A more basic condition, 10 M KOH, leads to higher C_2H_4 yield and lower onset overpotential for C_2H_4 production. It starts to generate 37% C_2H_4 at -0.3 V and reaches a peak of 66% C_2H_4 at -0.5 V. Clearly, by controlling electrolyte pH in the flow cell, our hybrid catalyst can deliver a further enhanced C_2H_4 FE from 40% (neutral) to 66% (10 M KOH) at a significantly decreased overpotential.

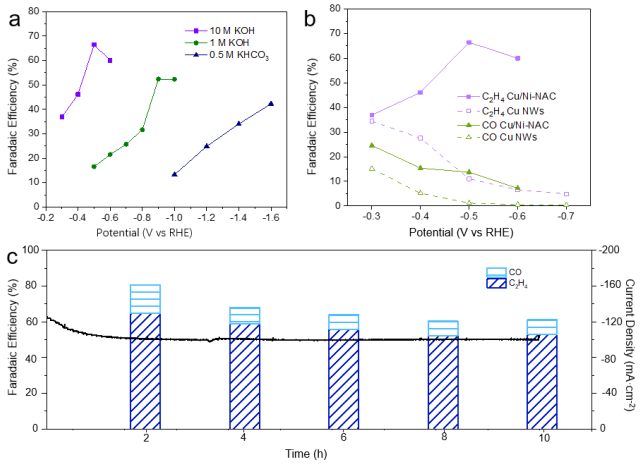

Figure 7. (a) eCO_2RR of Cu/Ni-NAC 10:1 in flow cells with different electrolytes. (b) Products distribution with Cu/Ni-NAC 10:1 and Cu NWs catalysts in flow cells (electrolyte: 10 M KOH). (c) eCO_2RR stability test of Cu/Ni-NAC 10:1 in a flow cell (electrolyte: 10 M KOH) .

To further demonstrate the synergy of two components in the hybrid catalyst, a control experiment with pure Cu NWs catalyst was carried out using the same flow cell condition (10 M KOH). We observed that Cu NWs behaves similarly as Cu/Ni-NAC 10:1 by enabling 30-40% C_2H_4 FE at -0.3 V (Figure 7b). However, at more negative overpotentials, the CO formation drops to nearly 0 with Cu NWs because of the significantly higher rate of competitive hydrogen evolution reaction. The lack of CO production leads to a dramatic drop in the C_2H_4 yield with Cu NWs. On the contrary, due to the high CO formation activity of Ni-NAC, the CO formation with the Cu/Ni-NAC catalyst remains higher than 10% at more negative potentials. With abundant CO intermediates, the Cu NWs in close contact with Ni-NAC remains high selectivity towards C_2H_4. In addition, the ability of Ni-NAC to generate sufficient CO within a wide potential range is further demonstrated upon the investigation of the Ni-NAC catalyst for eCO_2RR under the same alkaline conditions (Figure S9).

Meanwhile, we assessed our hybrid catalyst stability for the eCO_2RR in 10 M KOH (Figure 7c). After 10 hours of constant potential electrolysis at -0.5 V under the flow cell condition, the C_2H_4 FE drops slightly from 66% to 53%, while the current density remains above 100 $mA \cdot cm^{-2}$. Compared with recent Cu-based catalysts for eCO_2RR to ethylene, our hybrid catalyst stands out with both high selectivity and activity at low overpotentials (Table S1). Therefore, Cu/Ni-NAC 10:1 shows promise as a robust catalyst to selectively reduce CO_2 to C_2H_4 at low overpotentials.

EXPERIMENTAL SECTION

Chemicals. Nickel(II) acetylacetonate (95%), carbon tetrachloride (99.9%), ethylenediamine (99.5%), tetraethyl orthosilicate (TEOS, 98%), and pluronic P123 (Mn~5,800), oleylamine (OAm, >70%), copper(I) chloride(CuCl, 98%) were purchased from Sigma-Aldrich. Hydrofluoric acid (trace metal grade), hydrochloric acid (trace metal grade), nitric acid (trace metal grade) and N-Methyl-2-pyrrolidone (NMP) were purchased from Fisher Chemical. Platinum wire (0.5 mm diameter, Premion®, 99.997%) and Toray Carbon Paper (TGP-H-60) were obtained from Alfa Aesar. Polyvinylidene fluoride (PVDF) was purchased from MTI corporation. All chemicals were used as received without further purification.

Synthesis of Ni-NAC. Ni-NAC was synthesized according to our previous report.[42] In a typical synthesis, SBA-15 was obtained first for the template-growth of Ni-NAC. 4 g of pluronic P123 was firstly dissolved in 120 ml of hydrochloric solution (1.6 M) at 38 °C. After being dissolved, 8.5 ml of TEOS was added and the solution was kept stirring for 20 h. The composition of the achieved gel was: 1 TEOS: 0.017 P123: 5.68 HCl: 197 H_2O. The hydrothermal synthesis was performed in an oven at 100 °C for 24 h in a sealed polypropylene bottle. The white solid material was recovered by Büchner filtration, washed with distilled water, and dried overnight in an oven at 80 °C. The obtained solid was then calcined in a muffle furnace at 550 °C under air for 5 h with a heating rate of 1 °C min^{-1} to produce SBA-15. The Ni acetylacetonate was added into a solution of ethylenediamine (1.80 g) and carbon tetrachloride (4.00 g), followed by the addition of SBA-15 (0.80 g). The mixture was then heated in an oil bath set at 90 °C for 16 h for con-

densation before the oil bath temperature increased to 120 °C for 4 h to remove the uncondensed ethylenediamine and carbon tetrachloride. The obtained powders were calcined under Ar flow, with temperature raised in a ramping rate of 3 °C min^{-1} and further maintained at 800 °C for 2 h. The achieved black powder was then etched with 5 wt.% HF solution to remove the SBA-15. The catalyst was recovered via centrifuge, washed with deionized water until the pH reached 7. The catalyst was further dried at 100 °C for future usage.

Synthesis of Cu NWs. Cu NWs were synthesized using the reported method.[37] 0.1 g of CuCl was dissolved in 3 mL of OAm at 25 °C under Ar flow and vigorous magnetic stirring for 15 min. The solution was then heated to 120 °C for 30 min for degassing. After that, the reaction solution was heated to 180 °C at 20 °C min^{-1} and kept at this temperature for 90 min. After cooled down to room temperature, 40 mL of hexane was added to collect 50 nm wide Cu NWs via centrifugation (1000 rpm, 3 min). The product was purified by adding 40 mL of hexane and centrifugation for 3 times and then re-dispersed in hexane.

Synthesis Cu/Ni-NAC hybrid catalysts. The as-prepared Cu NWs (dissolved in hexane), Ni-NAC, and KJ Carbon are mixed in certain ratio and sonicate in hexane for 2 hours. The product was purified by adding 40 mL of hexane and centrifugation for 3 times and then dried in N_2 gas.

Characterization. Scanning electron microscope (SEM) imaging was obtained using the FEI Quanta 650 operated at 10 kV. Aberration corrected scanning transmission electron microscope (STEM) imaging was performed using the FEI Titan Themis. Powder X-ray diffraction (XRD) was carried out on a Bruker D8A25 diffractometer with Cu Kα radiation (λ = 1.54184 Å). N_2 physisorption was performed using an auto-adsorption analyzer (Micromeritics, 3Flex) at -196 °C. Inductively coupled plasma mass spectroscopy (ICP-MS) analysis for metal loadings was performed using Agilent 7700 ICP-MS. SEIRAS are collected by Thermo Scientific Nicolet iS50 FTIR Spectrometer. X-ray absorption spectroscopy (XAS) of the catalysts were measured at Beamline 9-BM of the Advanced Photon Source in Argonne National Laboratory. The in situ XANES spectra of Ni K-edges were collected at beamline 7-BM of the National Synchrotron Light Source II (NSLS-II) at Brookhaven National Laboratory. Details about the in situ XAS experiments can be referred to Ref. 48.

Electrode Preparation. 40 mg of the dried catalyst powder was ground with 4 mg of PVDF with a few drops of NMP to produce catalyst paste that was painted directly onto a 1.0 cm x 2.0 cm carbon paper. The catalyst-decorated carbon paper was dried in a vacuum-oven overnight and served as a working electrode.

eCO_2RR Test in H-cell. Autolab electrochemical potentiostat was used to conduct eCO_2RR experiments in aqueous 0.5 M $KHCO_3$. A platinum wire was used as the counter electrode. All potentials were measured against an Ag/AgCl reference electrode (4.0 M KCl, Pine instrument) and were converted to those against RHE. The experiments were performed in a gas-tight cell with two compartments separated by an anion exchange membrane (Nafion® 212). Each compartment contained 12 mL of electrolyte with approximately 10 mL of headspace. The deionized water was obtained from a Millipore Autopure System.

eCO_2RR Test in Flow Cell. Flow cell used for eCO_2RR is shown in Figure S8. A 2 cm × 2 cm Ni foam was used as the counter electrode. All potentials were converted to those against RHE. The experiments were performed in a gas-tight cell with two compartments separated by catalyst-loaded carbon paper/working electrode (the catalyst is loaded on the liquid phase side). The gas phase compartment is flowed by 10 sccm of CO_2 gas and the liquid phase compartment is filled by circulated 25 mL of electrolyte.

Product Analysis. Before the experiment, the electrolyte in the cathode compartment was saturated with CO_2 by bubbling CO_2 gas for at least 30 min and was stirred at 900 rpm. CO_2 gas was delivered at an average rate of 10 sccm (at room temperature and ambient pressure) and routed directly into the gas sampling loop of a gas chromatograph (SHIMADZU GC-2014). The gas phase composition was analyzed by GC every 35 min. The GC analysis was set up to split the gas sample into two aliquots whereof one aliquot was equipped with a thermal conductivity detector (TCD) for H_2 quantification. The second aliquot was equipped with a methanizer and a flame ionization detector (FID) for analyzing CO and C1 to C3 hydrocarbons. Argon (99.9999%) and hydrogen gas (99.9999%) were employed as carrier or make-up gases respectively. Solution ^1H NMR, acquired with Varian NMRS 600 MHz, was employed at the end of experiments to characterize liquid products. To be specific, 700 μL aliquot of the electrolyte was mixed with 70 μL of dimethyl sulfoxide (DMSO) standard solution (20 mM DMSO in D_2O).

CONCLUSIONS

In conclusion, we report a hybrid catalyst with complementary single-atom Ni and nanoscale Cu active modules that permits cascading CO_2-to-CO and CO-to-C_2H_4 processes for the efficient production of C_2H_4. Compared with traditional single-component catalysts, this modular design presents a novel and facile strategy for cross-module transfer and enriching key intermediate *CO onto the Cu surface for the C-C coupling to the desired product, as validated by *in situ* SEIRAS. The resultant Cu/Ni-NAC hybrid catalyst with optimized two module compositions produces C_2H_4 with 50% FE at -1.6 V vs. RHE in 0.5 M $KHCO_3$ solution and with 66% FE at -0.5 V vs. RHE in 10 M KOH condition. Moreover, the hybrid catalyst is durable under flow cell conditions. The highlighted modular design of the eCO_2RR catalyst is likely applicable to other catalytic applications that involve multiple steps with key intermediate formation and utilization occurring at distinct units.

ASSOCIATED CONTENT

Supporting Information. Additional figures (Figure S1-S9) and table (Table S1), including TEM, XRD characterizations, eCO_2RR product analysis, and cell design. This material is available free of charge via the Internet at http://pubs.acs.org.

AUTHOR INFORMATION

Corresponding Author

* jgchen@columbia.edu
* whuang@iastate.edu
* lqi@iastate.edu
* sz3t@virginia.edu

ACKNOWLEDGMENT

The work was supported by US National Science Foundation (CBET-2004808 and CHE-2145220). S.Z. acknowledges the support from a Scialog program (grant No. 28439) sponsored jointly by Research Corporation for Science Advancement and the Alfred P. Sloan Foundation, with additional support from Climate Pathfinders Foundation. L.Q. was supported by the U.S. Department of Energy (DOE), Office of Basic Energy Sciences, Division of Chemical Sciences, Geosciences, and Biosciences. The Ames Laboratory is operated for the U.S. DOE by Iowa State University under Contract No. DE-AC02-07CH11358. W.H. acknowledges the support from Trapp Innovation Award and Iowa State University. This research used 7-BM (QAS) beamline of the National Synchrotron Light Source II, with assistance by the Synchrotron Catalysis Consortium (U.S. DOE, Office of Basic Energy Sciences, Grant No. DE-SC0012335).

REFERENCES

(1) Pörtner, H.-O.; Roberts, D.C.; Tignor, M.; Poloczanska, E. S.; Mintenbeck, K.; Alegría, A.; Craig, M.; Langsdorf, S.; Löschke, S.; Möller, V.; Okem, A.; Rama, B. Climate change 2022: Impacts, adaptation, and vulnerability. *IPCC.* **2022**. 3056. doi:10.1017/9781009325844.

(2) Centi, G.; Perathoner, S. Opportunities and Prospects in the Chemical Recycling of Carbon Dioxide to Fuels. *Catal. Today* **2009**, *148*, 191–205.

(3) Appel, A. M.; Bercaw, J. E.; Bocarsly, A. B.; Dobbek, H.; Dubois, D. L.; Dupuis, M.; Ferry, J. G.; Fujita, E.; Hille, R.; Kenis, P. J. A.; Kerfeld, C. A.; Morris, R. H.; Peden, C. H. F.; Portis, A. R.; Ragsdale, S. W.; Rauchfuss, T. B.; Reek, J. N. H.; Seefeldt, L. C.; Thauer, R. K.; Waldrop, G. L. Frontiers, Opportunities, and Challenges in Biochemical and Chemical Catalysis of CO_2 Fixation. *Chem. Rev*. **2013**, 113, 6621–6658.

(4) Chen, C.; Kotyk, J. F. K.; Sheehan, S. W. Progress toward Commercial Application of Electrochemical Carbon Dioxide Reduction. *Chem* **2018**, *4*, 2571–2586.

(5) Jin, S.; Hao, Z.; Zhang, K.; Yan, Z.; Chen, J. Advances and Challenges for the Electrochemical Reduction of CO_2 to CO: From Fundamentals to Industrialization. *Angew. Chem. Int. Ed.* **2021**, *60*, 20627–20648.

(6) Wang, C.; Chen, J.; Ding, Y.; Cai, P.; Yi, L.; Li, Y.; Tu, C.; Hou, Y.; Wen, Z.; Dai, L. Electrocatalysis for CO_2 Conversion: From Fundamentals to Value-Added Products. *Chem. Soc. Rev.* **2021**, *50*, 4993–5061.

(7) Ross, M.B.; De Luna, P.; Li, Y.; Dinh, C.T.; Kim, D.; Yang, P.; Sargent, E.H. Designing materials for electrochemical carbon dioxide recycling. *Nat. Catal.* **2019**, 2(8), pp.648-658.

(8) Hori, Y.; Kikuchi, K.; Suzuki, S. Production of CO and CH_4 in Electrochemical Reduction of CO_2 at Metal-Electrodes in Aqueous Hydrogencarbonate Solution. *Chem. Lett.* **1985**, 11, 1695–1698.

(9) Yin, Z.; Palmore, G. T. R.; Sun, S. Electrochemical Reduction of CO2 Catalyzed by Metal Nanocatalysts. *Trends Chem*. **2019**, 1, 739-750.

(10) Todorova, T. K.; Schreiber, M. W.; Fontecave, M. Mechanistic Understanding of CO_2 Reduction Reaction (CO_2RR) Toward Multicarbon Products by Heterogeneous Copper-Based Catalysts. *ACS Catal.* **2020**, *10*, 1754–1768.

(11) Loiudice, A.; Lobaccaro, P.; Kamali, E. A.; Thao, T.; Huang, B. H.; Ager, J. W.; Buonsanti, R. Tailoring Copper Nanocrystals towards C_2 Products in Electrochemical CO_2 Reduction. *Angew. Chem. Int. Ed.* **2016**, *55*, 5789–5792.

(12) Huang, Y.; Handoko, A. D.; Hirunsit, P.; Yeo, B. S. Electrochemical Reduction of CO_2 Using Copper Single-Crystal Surfaces: Effects of CO* Coverage on the Selective Formation of Ethylene. *ACS Catal.* **2017**, *7*, 1749–1756.

(13) Luo, T.; Liu, K.; Fu, J.; Chen, S.; Li, H.; Hu, J.; Liu, M. Tandem Catalysis on Adjacent Active Motifs of Copper Grain Boundary for Efficient CO_2 Electroreduction toward C2 Products. *J. Energy Chem.* **2022**, *70*, 219–223.

(14) Choi, C.; Cheng, T.; Flores Espinosa, M.; Fei, H.; Duan, X.; Goddard 3rd, W. A.; Huang, Y. A Highly Active Star Decahedron Cu Nanocatalyst for Hydrocarbon Production at Low Overpotentials. *Adv. Mater.* **2018**, e1805405.

(15) Li, Y.; Cui, F.; Ross, M.B.; Kim, D.; Sun, Y.; Yang, P. Structure-sensitive CO_2 electroreduction to hydrocarbons on ultrathin 5-fold twinned copper nanowires. *Nano Lett.* **2017**, 17(2), pp.1312-1317.

(16) Shang, L.; Lv, X.; Zhong, L.; Li, S.; Zheng, G. Efficient CO_2 Electroreduction to Ethanol by Cu_3Sn Catalyst. *Small Methods* **2022**, *6*, 2101334.

(17) Ma, S.; Sadakiyo, M.; Heima, M.; Luo, R.; Haasch, R. T.; Gold, J. I.; Yamauchi, M.; Kenis, P. J. Electroreduction of Carbon Dioxide to Hydrocarbons Using Bimetallic Cu-Pd Catalysts with Different Mixing Patterns. *J. Am. Chem. Soc.* **2017**, *139*, 47–50.

(18) Kibria, M.G.; Dinh, C.T.; Seifitokaldani, A.; De Luna, P.; Burdyny, T.; Quintero-Bermudez, R.; Ross, M.B.; Bushuyev, O.S.; García de Arquer, F.P.; Yang, P.; Sinton, D. A surface reconstruction route to high productivity and selectivity in CO_2 electroreduction toward C2+ hydrocarbons. *Adv. Mater.* **2018**, 30(49), 1804867.

(19) De Luna, P.; Quintero-Bermudez, R.; Dinh, C.T.; Ross, M.B.; Bushuyev, O.S.; Todorović, P.; Regier, T.; Kelley, S.O.; Yang, P.; Sargent, E.H. Catalyst electro-redeposition controls morphology and oxidation state for selective carbon dioxide reduction. *Nat. Catal.* **2018**, 1(2), 103-110.

(20) Merino-Garcia, I.; Albo, J.; Solla-Gullon, J.; Montiel, V.; Irabien, A. Cu oxide/ZnO-based surfaces for a selective ethylene production from gas-phase CO2 electroconversion. *J. CO2 Util.* **2019** 31, 135-142.

(21) Chen, X.; Chen, J.; Alghoraibi, N. M.; Henckel, D. A.; Zhang, R.; Nwabara, U. O.; Madsen, K. E.; Kenis, P. J. A.; Zimmerman, S. C.; Gewirth, A. A. Electrochemical CO_2-to-Ethylene Conversion on Polyamine-Incorporated Cu Electrodes. *Nat. Catal.* **2020**, *4*, 20–27.

(22) Santos-Lorenzo, J.; San José-Velado, R.; Albo, J.; Beobide, G.; Castano, P.; Castillo, O.; Luque, A.; Pérez-Yáñez, S.; A straightforward route to obtain zirconium based metal-organic gels. *Micropor. Mesopor. Mat.* **2019** 284, 128-132.

(23) Albo, J.; Maite, P. I.; Garikoitz, B.; Angel I. Cu/Bi metal-organic framework-based systems for an enhanced electrochemical transformation of CO2 to alcohols. *J. CO2 Util.* **2019**, 33, 157-165.

(24) Perfecto-Irigaray, M.; Albo, J.; Beobide, G.; Castillo, O.; Irabien, A.; Pérez-Yáñez, S. Synthesis of heterometallic metal–organic frameworks and their performance as electrocatalyst for CO 2 reduction. *RSC Adv.* **2018**, 18, 21092-21099.

(25) Albo, J.; Vallejo, D.; Beobide, G.; Castillo, O.; Castaño, P.; Irabien, A.; Copper‐based metal‐Organic porous materials for CO2 electrocatalytic reduction to alcohols. *ChemSusChem* **2017**, 6, 1100-1109.

(26) Dinh, C.-T.; Burdyny, T.; Kibria, M. G.; Seifitokaldani, A.; Gabardo, C. M.; Garcia de Arquer, F. P.; Kiani, A.; Edwards, J. P.; De Luna, P.; Bushuyev, O. S.; Zou, C.; Quintero-Bermudez, R.; Pang, Y.; Sinton, D.; Sargent, E. H. Carbon Dioxide Electroreduction to Ethylene via Hydroxide-Mediated Copper Catalysis at an Abrupt Interface. *Science* **2018**, *360*, 783–787.

(27) Salvatore, D.; Gabardo, C.; Reyes, A.; Salvatore, D. A.; Gabardo, C. M.; O, C. P.; Holdcroft, S.; Pintauro, P.; Bahar, B.; Hickner, M.; Bae, C.; Sinton, D.; Sargent, E. H.; Berlinguette, C. P. Designing Anion Exchange Membranes for CO_2 Electrolysers. *Nat. Energy*. **2021**, 6, 339-348.

(28) Mu, S.; Lu, H.; Wu, Q.; Li, L.; Zhao, R.; Long, C.; Cui, C. Hydroxyl radicals dominate reoxidation of oxide-derived Cu in electrochemical CO2 reduction. *Nat. Commun.* **2022**, 13, 1-8.

(29) Lei, Q.; Zhu, H.; Song, K.; Wei, N.; Liu, L.; Zhang, D.; Yin, J.; Dong, X.; Yao, K.; Wang, N.; Li, X. Investigating the origin of enhanced C2+ selectivity in oxide-/hydroxide-derived copper electrodes during CO2 electroreduction. *J. Am. Chem. Soc.* **2022**, 142, 4213-4222.

(30) Jeong, H.M.; Kwon, Y.; Won, J.H.; Lum, Y.; Cheng, M. J.; Kim, K.H.; Head-Gordon, M.; Kang, J. K. Atomic‐Scale Spacing between Copper Facets for the Electrochemical Reduction of Carbon Dioxide. Adv. Energy Mater. **2020**, 10, 1903423.

(31) Varandili, S. B.; Huang, J.; Oveisi, E.; De Gregorio, G.L.; Mensi, M.; Strach, M.; Vavra, J.; Gadiyar, C.; Bhowmik, A.; Buonsanti, R. Synthesis of Cu/CeO2-x nanocrystalline heterodimers with interfacial active

sites to promote CO2 electroreduction. *ACS Catal.* **2019**, 9, 5035-5046.

(32) Zhou, Y.; Che, F.; Liu, M.; Zou, C.; Liang, Z.; De Luna, P.; Yuan, H.; Li, J.; Wang, Z.; Xie, H.; Li, H. Dopant-induced electron localization drives CO2 reduction to C2 hydrocarbons. *Nat. Chem.* **2018**, 10, 974-980.

(33) Su, X.; Jiang, Z.; Zhou, J.; Liu, H.; Zhou, D.; Shang, H.; Ni, X.; Peng, Z.; Yang, F.; Chen, W.; Qi, Z. Complementary Operando Spectroscopy identification of in-situ generated metastable charge-asymmetry Cu2-CuN3 clusters for CO2 reduction to ethanol. *Nat. Commun.* **2022**, 13, 1-11.

(34) Rossi, K.; Buonsanti, R. Shaping Copper Nanocatalysts to Steer Selectivity in the Electrochemical CO_2 Reduction Reaction. *Acc. Chem. Res.* **2022**, *55*, 629–637.

(35) Xiao, C.; Zhang, J. Architectural Design for Enhanced C2 Product Selectivity in Electrochemical CO_2 Reduction Using Cu-Based Catalysts: A Review. *ACS Nano* **2021**, *15*, 7975–8000.

(36) Suo, H.; Solan, G. A.; Ma, Y.; Sun, W. H. Developments in Compartmentalized Bimetallic Transition Metal Ethylene Polymerization Catalysts. *Coord. Chem. Rev.* **2018**, *372*, 101–116.

(37) Zhang, H.; Zhang, Y.; Li, Y.; Ahn, S.; Palmore, G. T. R.; Fu, J.; Peterson, A. A.; Sun, S. Cu Nanowire-Catalyzed Electrochemical Reduction of CO or CO_2. *Nanoscale* **2019**, *11*, 12075–12079.

(38) Wang, L.; Nitopi, S. A.; Bertheussen, E.; Orazov, M.; Morales-Guio, C. G.; Liu, X. Y.; Higgins, D. C.; Chan, K. R.; Norskov, J. K.; Hahn, C.; Jaramillo, T. F. Electrochemical Carbon Monoxide Reduction on Polycrystalline Copper: Effects of Potential, Pressure, and PH on Selectivity toward Multicarbon and Oxygenated Products. *ACS Catal.* **2018**, *8*, 7445–7454.

(39) An, H.; Wu, L.; Mandemaker, L. D. B.; Yang, S.; de Ruiter, J.; Wijten, J. H. J.; Janssens, J. C. L.; Hartman, T.; van der Stam, W.; Weckhuysen, B. M. Sub-Second Time-Resolved Surface-Enhanced Raman Spectroscopy Reveals Dynamic CO Intermediates during Electrochemical CO_2 Reduction on Copper. *Angew. Chem. Int. Ed.* **2021**, *60*, 16576–16584.

(40) Raciti, D.; Cao, L.; Livi, K. J. T.; Rottmann, P. F.; Tang, X.; Li, C.; Hicks, Z.; Bowen, K. H.; Hemker, K. J.; Mueller, T.; Wang, C. Low-Overpotential Electroreduction of Carbon Monoxide Using Copper Nanowires. *ACS Catal.* **2017**, *7*, 4467–4472.

(41) Nitopi, S.; Bertheussen, E.; Scott, S. B.; Liu, X.; Engstfeld, A. K.; Horch, S.; Seger, B.; Stephens, I. E. L.; Chan, K.; Hahn, C.; Nørskov, J. K.; Jaramillo, T. F.; Chorkendorff, I. Progress and Perspectives of Electrochemical CO_2 Reduction on Copper in Aqueous Electrolyte. *Chem. Rev.* **2019**, *119*, 7610–7672.

(42) Luo, Z.; Yin, Z.; Yu, J.; Yan, Y.; Hu, B.; Nie, R.; Kolln, A. F.; Wu, X.; Behera, R. K.; Chen, M.; Zhou, L.; Liu, F.; Wang, B.; Huang, W.; Zhang, S.; Qi, L. General Synthetic Strategy to Ordered Mesoporous Carbon Catalysts with Single-Atom Metal Sites for Electrochemical CO_2 Reduction. *Small* **2022**, 2107799.

(43) Luo, Z.; Nie, R.; Nguyen, V. T.; Biswas, A.; Behera, R. K.; Wu, X.; Kobayashi, T.; Sadow, A.; Wang, B.; Huang, W.; Qi, L. Transition Metal-like Carbocatalyst. *Nat. Commun.* **2020**, *11*, 1–9.

(44) Grosse, P.; Gao, D.; Scholten, F.; Sinev, I.; Mistry, H.; Roldan Cuenya, B. Dynamic Changes in the Structure, Chemical State and Catalytic Selectivity of Cu Nanocubes during CO_2 Electroreduction: Size and Support Effects. *Angew. Chem. Int. Ed.* **2018**, *57*, 6192–6197.

(45) Mukherjee, S.; Yang, X.; Shan, W.; Samarakoon, W.; Karakalos, S.; Cullen, D. A.; More, K.; Wang, M.; Feng, Z.; Wang, G.; Wu, G. Atomically Dispersed Single Ni Site Catalysts for Nitrogen Reduction toward Electrochemical Ammonia Synthesis Using N_2 and H_2O. *Small Methods* **2020**, *4*, 1900821.

(46) Dunwell, M.; Lu, Q.; Heyes, J. M.; Rosen, J.; Chen, J. G.; Yan, Y.; Jiao, F.; Xu, B. The Central Role of Bicarbonate in the Electrochemical Reduction of Carbon Dioxide on Gold. *J. Am. Chem. Soc.* **2017**, *139*, 3774–3783.

(47) Gunathunge, C. M.; Ovalle, V. J.; Li, Y.; Janik, M. J.; Waegele, M. M. Existence of an Electrochemically Inert CO Population on Cu Electrodes in Alkaline PH. *ACS Catal.* **2018**, *8*, 7507–7516.

(48) Lee, J.H.; Kattel, S.; Jiang, Z.; Xie, Z.; Yao, S.; Tackett, B.M.; Xu, W.; Marinkovic, N.S.; Chen, J.G., Tuning the activity and selectivity of electroreduction of CO_2 to synthesis gas using bimetallic catalysts. *Nat. Commun.* **2019**, 10, 1-8.

Table of Contents